

Solar Eclipse Observations from the Ground and Air from 0.31 to 5.5 Microns

 $\begin{array}{l} Philip\ Judge^1 @ \cdot Ben\ Berkey^1 \cdot Alyssa\ Boll^2 \cdot Paul\ Bryans^1 \cdot Joan\ Burkepile^1 \cdot \\ Peter\ Cheimets^3 \cdot Edward\ DeLuca^3 \cdot Giuliana\ de\ Toma^1 \cdot Keon\ Gibson^4 \cdot \\ Leon\ Golub^3 \cdot James\ Hannigan^5 \cdot Chad\ Madsen^3 \cdot Vanessa\ Marquez^3 \cdot \\ Austin\ Richards^6 \cdot Jenna\ Samra^3 \cdot Scott\ Sewell^1 \cdot Steven\ Tomczyk^1 \cdot Alysha\ Vera^7 \end{array}$

Received: 22 August 2019 / Accepted: 24 October 2019 / Published online: 27 November 2019 © Springer Nature B.V. 2019

Abstract We present spectra and broad-band polarized light data from a novel suite of instruments deployed during the 21st August 2017 total solar eclipse. Our goals were to survey solar spectra at thermal infrared wavelengths during eclipse, and to test new technology for measuring polarized coronal light. An infrared coronal imaging spectrometer, flown at 14.3 km altitude above Kentucky, was supported on the ground by observations from Madras, Oregon (elevation 683 m) and Camp Wyoba on Casper Mountain, Wyoming (2402 m). In Wyoming we deployed a new infrared Fourier Transform Spectrometer (FTS), three low-dispersion spectrometers loaned to us by Avantes, a novel visible-light camera PolarCam, sensitive to linear polarization, and one of two infrared cameras from FLIR Systems, the other operated at Madras. Circumstances of eclipse demanded that the observations spanned 17:19 to 18:26 UT. We analyze spectra of the limb photosphere, the chromosphere, prominences, and coronal lines from 310 nm to 5.5 µm. We calibrated data photometrically using the solar disk as a source. Between different spectrometers, the calibrations were consistent to better than 13%. But the sensitivities achieved were insufficient to detect coronal lines from the ground. The PolarCam data are in remarkable agreement with polarization data from the K-Cor synoptic instrument on Mauna Loa, and with FLIR intensity data acquired in Madras. We discuss new results, including a detection of the He I 1083 nm multiplet in emission during the whole of totality. The combination of the FTS and AIR-Spec spectra reveals for the first time the effects of the telluric extinction on the infrared coronal emission lines, to be observed with upcoming Daniel K. Inouye Solar Telescope.



High Altitude Observatory, National Center for Atmospheric Research, PO Box 3000, Boulder, CO 80307, USA

Colorado School of Mines, 1500 Illinois St, Golden, CO 80401, USA

Smithsonian Astrophysical Observatory, 60 Garden St, Cambridge, MA 02138, USA

Jackson State University, 1400 John R. Lynch St, Jackson, MS 39217, USA

⁵ ACOM, National Center for Atmospheric Research, PO Box 3000, Boulder, CO 80307, USA

FLIR Systems, 5951 Encina Road, Suite 202, Goleta, CA 93117, USA

⁷ Smith College, Northampton, MA 01063, USA

166 Page 2 of 23 P. Judge *et al.*

Keywords Sun: corona · Sun: chromosphere · Sun: infrared

1. Introduction

The "mystery of the solar atmosphere" (Hoyle, 1955), why coronal plasma is so hot, was one of the outstanding problems in 20th century physics, and it remains so into the 21st century (*e.g.* Golub and Pasachoff, 2009; Sakurai, 2017). Two things we know for certain are that coronal physics is intimately tied to the evolving solar magnetic field, and that there is plenty of energy available. The difficulties are to identify the modes by which energy is transported and dissipated. The corona is also the site of slow magnetic energy storage and sudden release, manifested in violent flares and "coronal mass ejections" (CMEs). These events have profound impacts on the terrestrial system (*e.g.* Eddy, 2009).

Prompted in part by societal needs, solar physicists agree that we must take on the difficult problem of measuring the magnetic field in the corona, in order to understand better the sources and causes of the dynamic solar events (*e.g.* Casini, White, and Judge, 2017). Partly in response to this need, the United States is constructing the 4-meter *Daniel K. Inouye Solar Telescope* (DKIST), a facility to begin operations in late 2019. It is the first major facility for ground-based solar physics in the USA since the mid 1960s. However, the coronal infrared spectrum over the range of wavelengths observable by DKIST remains sparsely sampled. The total eclipse of 2017 offered a timely opportunity to explore this wavelength space in advance of DKIST operations.

Münch, Neugebauer, and McCammon (1967) were among the first to use high-altitude aircraft to observe coronal lines in the mid-infrared region. Our motivation is in part the same as Münch, Neugebauer, and McCammon (1967):

"...the wavelengths of the lines cannot be predicted with sufficient precision to evaluate the effects of telluric absorption on their intensities at ground locations...observation from a high-altitude aircraft offered definite advantages..."

Our choice was therefore to fly a moderate resolution spectrograph, taking advantage of a new 2D camera system, on a high-altitude modern aircraft, and to support this experiment using instruments on the ground. In particular, high resolution spectra obtained with the new *NCAR Airborne Interferometer*, a Fourier Transform Spectrometer (FTS) instrument, permit us to assess the detailed telluric absorption profile for each new emission line measured from the aircraft. The coronal lines beyond 2 microns have poorly known wavelengths, being determined mostly from the Ritz principle from EUV lines (*e.g.* Judge *et al.*, 2001), with the exception of a line of [Si IX] at 3.93434 ± 0.00007 microns (Judge *et al.*, 2002). A secondary motivation was to search the infrared (IR) region for magnetically-sensitive coronal lines. Since *ca.* 1990, observations of emission lines of the near infrared corona have been used to measure properties of the spectrum and coronal magnetic field (Penn and Kuhn, 1994,b; Penn *et al.*, 1994; Kuhn, Penn, and Mann, 1996; Lin, Penn, and Tomczyk, 2000; Judge *et al.*, 2002).

Figure 1 presents a low-dispersion overview of uncalibrated (upper panel) and calibrated infrared spectra (lower panel) of the partially-eclipsed Sun acquired using three instruments. These were obtained during the 70 seconds before second contact ("C2"). The figure shows several bright emission lines predominantly from hydrogen from prominences and the solar chromosphere, from the NAI instrument (upper panel, note that it was deployed on the ground). In the lower panel, data from three spectrographs are shown, revealing the telluric absorption bands, the astronomical transmission bands, and identifies the main telluric



Eclipse Observations Page 3 of 23 166

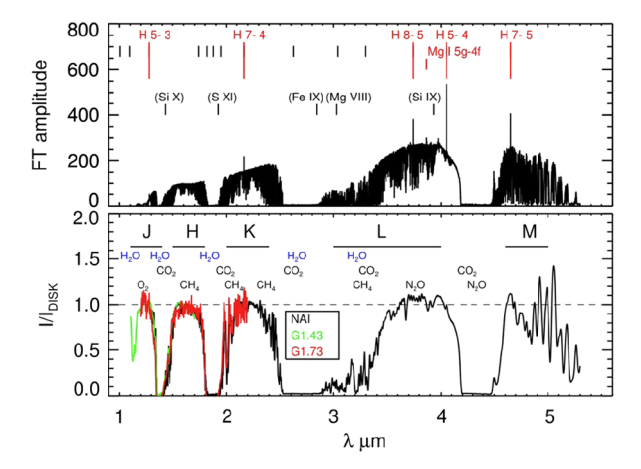


Figure 1 Spectra of the partial solar disk prior to second contact from the *NCAR Airborne Interferometer* (NAI), a Fourier Transform Spectrometer that was deployed on the ground, are compared with the "Fcal" data (see text) from the G1.43 and G1.73 instruments. All data were obtained before second contact. The *upper panel* shows spectra at one half of the full NAI resolution (0.36 cm⁻¹ wavenumbers). Chromospheric/prominence emission lines of H and Mg are identified in *red*. Those marked in *black* were not detected, even during totality. Notably, no coronal line was detected. The locations of the AIR-Spec emission lines (those marked in *brackets*) are marked in the *upper panel*. In the *lower panel*, the NAI data are reduced to a resolution varying from 700 to 5000 (as shown, it is constant in wavenumbers, 15 cm⁻¹). All data in the *lower panel* are normalized to the continuum disk-center intensity. Astronomical J-M bands and dominant molecular atmospheric absorbers are identified in the *lower panel*. Labels G1.43 and G1.73 refer to two of three Avantes spectrometers (Section 2).

molecular absorbers. The lower spectra are calibrated so that unattenuated disk center spectra would equal one, as described below. The NAI spectrum has been smoothed in wavenumber space with a Gaussian profile of width of 15 wavenumbers, for an easier comparison with the Avantes data. The relative calibrations (discussed below) typically give results mutually consistent to better than \pm 13%, between the Avantes and NAI data. We regard this as excellent agreement given the rather crude nature of our calibration procedure.

The spectrum of the visible and infrared corona alone is that of the F- (dust) and K- (electron-scattered) continua, superimposed with very shallow and broad absorption features, formed by scattering of photospheric light by the electrons (Grotrian, 1933). On top of this is the E-corona (emission lines), formed by a mix of scattered photospheric light and thermal emission from atomic ions. Both are only visible during a total solar eclipse or with a coronagraph. It is important to stress that no coronal features are visible in Figure 1, because of the dominance of disk light from the narrow crescents before totality. In fact, even during totality, coronal emission lines were only detected from the aircraft experiment reported below (see also Samra, 2018; Samra *et al.*, 2018).

In spite of the well-known but variable telluric absorption (between the J, H, K, L and M bands seen in Figure 1), the infrared region has potential benefits over visible light for coronal work. While predictions are available (*e.g.* Münch, Neugebauer, and McCammon, 1967; Judge, 1998; Judge *et al.*, 2002; Del Zanna and DeLuca, 2018), the coronal spectrum above 1 micron is only sparsely explored out to 4 microns, completely unexplored above this. On the plus side, magnetic sensitivities are stronger, the atmospheric seeing much improved, and the atmospheric brightness far less.

The total eclipse of 21 August 2017, with maximum over the continental USA, presented an excellent opportunity for new eclipse campaigns. Table 1 lists the experiments that we



166 Page 4 of 23 P. Judge *et al.*

Table 1 Summary of experiments.

Name	Description	Prime objective	Investigators
AIR-Spec*	Airborne slit spectrometer	IR spectra of corona and chromosphere	E. DeLuca J. Samra P. Cheimets
NAI [†]	Fourier transform interferometer	$\mathcal{R} > 10^4$ spectrum of the Sun from 2 to 5 microns	J. Hannigan S. Sewell P. Bryans
Avantes	Low-resolution spectrographs	Rapid-acquisition flash and coronal spectra	S. Tomczyk P. Judge
FLIR [‡]	FLIR camera plus broad and narrow filters	Thermal IR images of the corona	S. Tomczyk K. Gibson B. Berkey
FLIR#	FLIR camera plus narrow-band filter	Si IX 3.95 μm images of the corona	A. Richards
PolarCam	Imaging polarimeter	Linear polarization of K-corona	S. Tomczyk A. Boll J. Burkepile G. de Toma

All instruments were operated before, during and after totality. *Deployed on NCAR's HIAPER Gulfstream V aircraft. †Designed for aircraft use, this instrument was deployed, along with FLIR, PolarCam and the three Avantes spectrographs, (G0.70, G1.43 and G1.73) on the ground at Camp Wyoba. *Spectrographs generously loaned by Avantes corporation. ‡On loan from FLIR corporation. #Deployed at Madras, Oregon.

performed, with their main objectives. Most of the objectives were met, except (1) that the FLIR camera at Camp Wyoba lost focus before totality, and (2) our instruments on the ground lacked the sensitivity and thermal stability needed to detect coronal lines, during the rapidly changing ground conditions of total eclipse. The latter was not unexpected, given limited resources available to us. Nevertheless, useful results are reported below inside and outside of totality, using the unique combination of instruments.

Figure 2 shows the geometry of the eclipse as seen from Camp Wyoba, superposed with entrance slits for the two instruments for which slits or slots were used. Camp Wyoba is roughly 10 km south of the centerline of the Moon's shadow.

2. Eclipse Experiments

The suite of ground-based instruments, except for the much larger NAI instrument housed in its own trailer, is shown in Figure 3. To understand the data from the diverse set of instruments, it is helpful to show first not only the low-resolution photospheric spectra in the lower panel of Figure 1, but also the sensitivities achieved by each instrument. Figure 4 compares the sensitivities achieved, using procedures described below and, for the Avantes and NAI spectrographs, in a companion paper by Judge *et al.* (2019). Here we refer to the Avantes spectrographs and spectra using the labels " $G\lambda$ ", *i.e.* G0.70, G1.43, G1.73, where λ



Eclipse Observations Page 5 of 23 166

Figure 2 A Sobel-enhanced PolarCam polarized brightness (pB) coronal image is shown in relative equatorial coordinates, superimposed with data for the lunar trajectory and the slot and slit positions for the Avantes and AIR-Spec instruments, respectively. The AIR-Spec data were acquired roughly 40 minutes after this image was obtained. The color table is reversed for clarity.

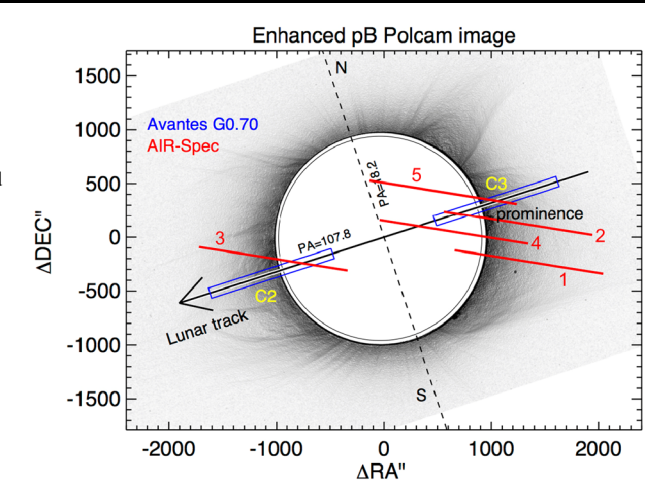


Figure 3 Five of the six experiments on the ground at Camp Wyoba are shown in front of the tent containing spectrographs, computers and operators. Three of the experiments are fed by the "Avantes telescopes".

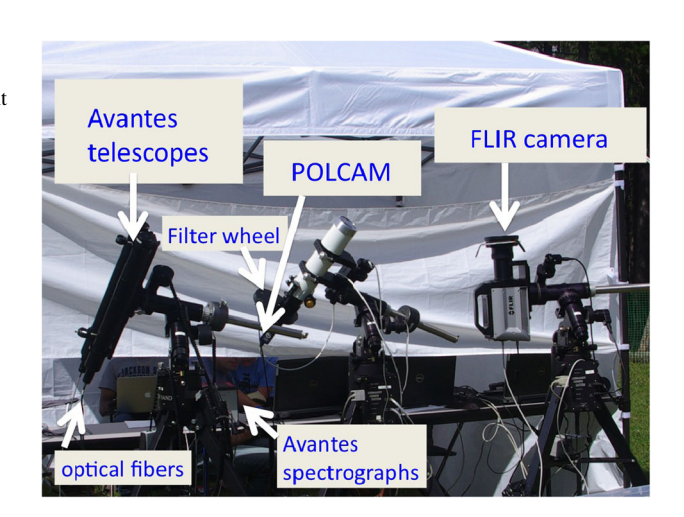
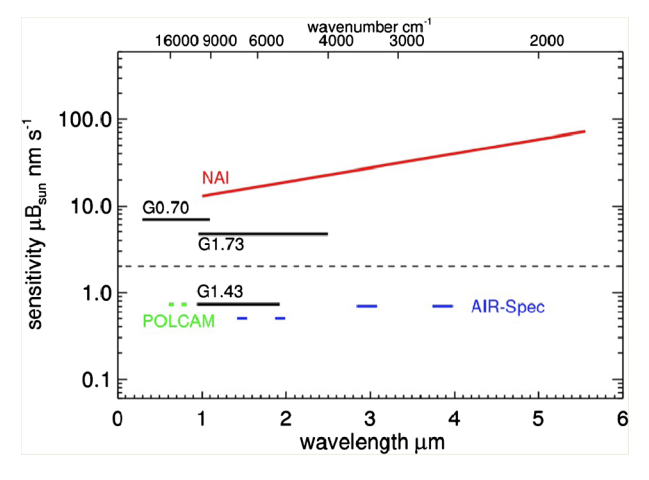


Figure 4 The estimated sensitivities of the instruments are plotted against wavelength. The lines plotted span the wavelengths covered by each instrument and mode. The dashed line shows a brightness of 2×10^{-6} of the disk brightness, indicating the typical brightness of the corona just above the limb. The sensitivities are for a bandpass of 1 nm and for an integration time of 1 second. The sensitivities strictly apply only near the centers of the spectral bands shown, for the Avantes data.





166 Page 6 of 23 P. Judge *et al.*

is the central wavelength in μm of the grating. These sensitivities are only rough estimates owing to the difficulty of assessing the significant role of thermal changes in instruments over the eclipse. They apply, for the spectrographs, to a 1 second exposure, integrated over 1 nm of the spectrum. It should be noted that the emission lines observed are between 4 to 20 times narrower than this bandwidth. Further, the sensitivities cannot naïvely be scaled as the inverse square root of the exposure time, owing to systematic sources of uncertainty and secular thermal changes in the instruments. In spite of these issues, this sensitivity chart is compatible with detections and non-detections of the continuum corona (shown as a dashed horizontal line) during totality.

We performed "Sun-to-detector" calculations for the Avantes instruments based upon instrumental setups and spectrometer data listed in the Avantes catalog ("Avantes Catalog X.pdf", at https://www.avantes.com/catalog/). The count rates acquired are $\approx 30\%$ larger than those expected for a system with a 100% efficiency. For example, the G1.43 instrument accumulated 4300 net counts per 0.5 second exposure in the corona, compared with the predicted value of 6000 for an average coronal brightness of 0.8 millionths at solar minimum (Allen, 1973). This is reassuringly good agreement. However, measured sensitivity levels achieved are significantly above those from photon counting. A significant contribution comes from the course 16-bit A to D conversion (over 2000 photons per count), and to the warm detectors, which increase noise levels and, under eclipse conditions, introduce variable responses to changing temperatures. As a result, measured sensitivities are above those from counting statistics, by roughly an order of magnitude. We suspect that the variable thermal conditions and perhaps other sources of systematic error (non-linear pixel-to-pixel variations, variable dark frames, and the absence of available flat-field frames) have limited our ability to detect weak features, such as coronal lines.

We chose to feed the light afocally to each ground-based spectrograph, by picking light from a collimated beam (Avantes) or simply directing sunlight into the NAI instrument using a heliostat mirror. The only spatial information is contained in the times relative to C2 (second contact) and C3 (third contact), because in this configuration we simply measure total flux from the field of view of each instrument. This choice was made to provide a high quality signal as a function of time which, in the absence of clouds, is far less dependent of seeing conditions than the usual flash-spectrum technique (see Judge *et al.*, 2019).

In Figure 2 we show the positions of the slit of the AIR-Spec imaging spectrograph instrument flown on the NCAR GV aircraft. From its base in Chattanooga, the airplane took off shortly before the eclipse, then flew north and east to intercept the Moon's shadow at an altitude of around 45 000 feet over Kentucky. The high altitude of the aircraft was critical to removing telluric absorption features and to removing nearly all scattered atmospheric light. Aircraft maneuverability was desirable to chase the Moon's shadow, just 100 km wide, and the high platform velocity of the GV extended the totality duration from 2.5 to approximately 4 minutes. AIR-Spec was the only spectrometer stable and sensitive enough to detect coronal emission lines.

2.1. At Camp Wyoba

Our station at Camp Wyoba (Longitude W 106° 19′ 17.0″, Latitude N 42° 44′ 5.0″, altitude \approx 2422 m) was situated on Casper Mountain, Wyoming. Second contact was at 17:42:37.2 UT, third at 17:45:04.1 UT, computed from the Naval Observatory eclipse calculator. These timings were confirmed by visual observations to within roughly 1 second. Totality duration was \approx 147 seconds, eclipse magnitude 1.013. Cirrus, present tens of minutes before second contact, moved from the solar disk before totality. By eye, the sky ap-



Eclipse Observations Page 7 of 23 166

peared clear during all observations presented here. The corona appeared bright, sharp and unattenuated to the dark-adapted eyes of all on the ground.

Table 1 briefly lists our experiments, their principal aims, and the responsible personnel. We fielded an infrared camera generously loaned to us by FLIR corporation. However, the results were compromised by uncorrected secular changes of focus which were exacerbated by the fast f/2.5 optics, resulting from rapidly changing temperatures. We were unable to derive results of scientific value from this instrument.

2.1.1. NAI Fourier Transform Spectrometer

The NCAR Airborne Interferometer was designed by one of us (J.H.) and constructed and operated by J.H. and S.S. It was deployed from a trailer in the same field at Camp Wyoba as the other experiments.

The NAI FTS was designed to build upon earlier middle infrared (mid-IR) solar transmission spectral measurements of the terrestrial atmosphere that have been performed on aircraft at NCAR for many years (e.g. Coffey, Hannigan, and Goldman, 2006). The original acquisition and resolution specifications allow the NAI to be a traveling transfer standard for ground-based spectroscopy. In particular, it can serve as a standard for the Network for the Detection of Atmospheric Composition Change (NDACC) (De Mazière et al., 2018). Re-purposing the instrument for the eclipse entailed several modifications. The basic optical design of the 4× folding Michelson interferometer allowed us to reposition the center burst in the optical path. The center burst is the signal measured at zero path difference. Since all waves then combine constructively, it is the total energy passing through the instrument so the largest signal that rapidly falls off as the path difference increases. We were able to take 10 cm symmetric interferograms in just 2.5 seconds. To include > 90% of the coronal flux the instrumental field of view (FOV) was increased to 1.5° or about $3\times$ the apparent solar diameter, with an acceptance aperture enlarged to 11.6 mm diameter. Tracking the Sun as it traverses the sky is often performed with some dynamical feedback using the bright solar disk. Not being an option during totality, we adopted an ephemeris-only driven tracking system with direct injection of the parallel solar beam into the instrument. This configuration has advantages of less photon loss with fewer reflections, and no vignetting of the beam, at the expense of limiting the duration of stability due to the static tracker. The team was able to make continuous scans, locked on the eclipsed solar disk for 210 seconds. They successfully acquired nine scans before totality, 60 during, and 13 afterwards. The corona was too dim for the NAI to obtain useful data during totality. Before and after totality useful data between 1 and 5.5 µm were obtained. Figure 1 shows smoothed raw and calibrated NAI data obtained between 17:42:17 and 17:42:38 UT, 20 seconds before and 1 second after second contact. The data shown are the average of the nine 2.5-second scans obtained over this period. These separate scans are all qualitatively similar (examples are shown in Figure 3 of Judge et al., 2019). Changing light levels during the 2.5-second scans should have an insignificant effect on the spectra, for our simple exploration of the telluric and solar absorption and emission spectra during eclipse. Such problems are reduced in double-sided interferograms, as the center burst (maximum energy) is in the middle of the scan period.

To assess the effects of variation in brightness, we note that during the first NAI scan, the theoretical flux changes by 12.5% from beginning to end (the brightness change is linear in time in Figure 5 near 20 seconds). In contrast, near 5 seconds the change is 50%, yet the spectra are qualitatively similar. Figure 3 of Judge *et al.* (2019) shows the reproducibility of fine structure in the spectra, from 1.28 to 4.66 microns over 10 narrow passbands. Figure 6 shows that the broad structure of the spectra are also, where solar light is present, very



166 Page 8 of 23 P. Judge *et al.*

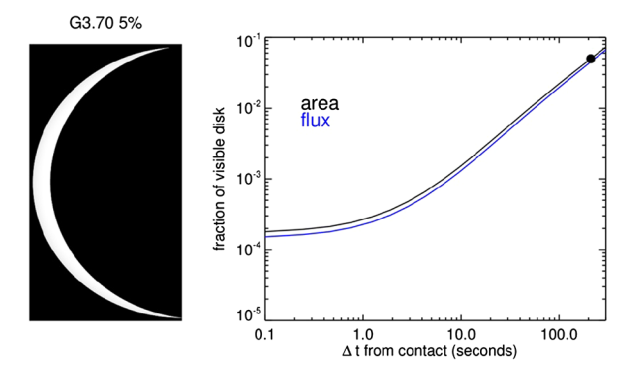
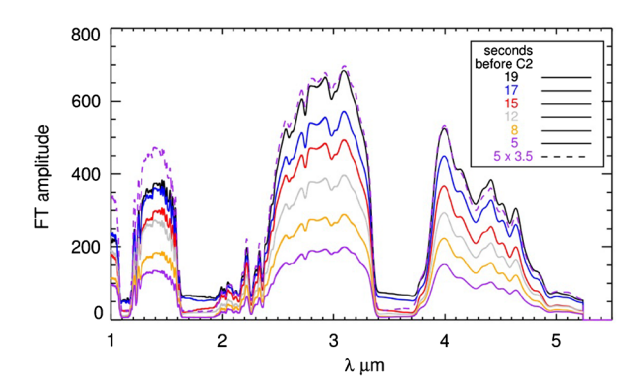


Figure 5 The *right panel* shows the fractions of the visible disk and the fractional flux as a function of the absolute difference time from second or third contact. The *left panel* shows the solar disk intensity computed when 5% of the disk is visible (this time is marked with a *black circle in the right hand panel*). These calculations were used to obtain calibrated fluxes and intensities relative to the solar disk-center intensity for the afocal spectrometer experiments.

Figure 6 The time dependence of the NAI counts, smoothed by a factor of 200 over the native resolution, is shown as second contact is approached. The *dashed line* shows 3.5 times the counts obtained 5 seconds before C2, highlighting the systematic errors probably induced by increasing time variability in flux as C2 is approached.



similar. The changes in spectra between the 19 and 5 second scans are evident on scales of the lowest wavenumbers ($\approx 1 \text{ micron}^{-1}$), such as differences in the darkest regions between the astronomical J through M bands, and in the 1.4 micron J band.

The raw data were Fourier transformed and processed by JH, and then calibrated in brightness through models for the limb darkening (Allen, 1973), which when integrated, yield the flux f_{λ} emerging from the visible crescents during the approach to C2. One example is shown in Figure 5 for calculations at 3.70 μ m. The model used circular disks for the Sun and Moon, with the center of the Moon displaced by 5" to the celestial north owing to the site's location south of the central line of eclipse. As a result the crescent in the left panel is slightly tilted. The flux and area curves are very similar at 3.7 μ m shown, because the limb darkening is small.

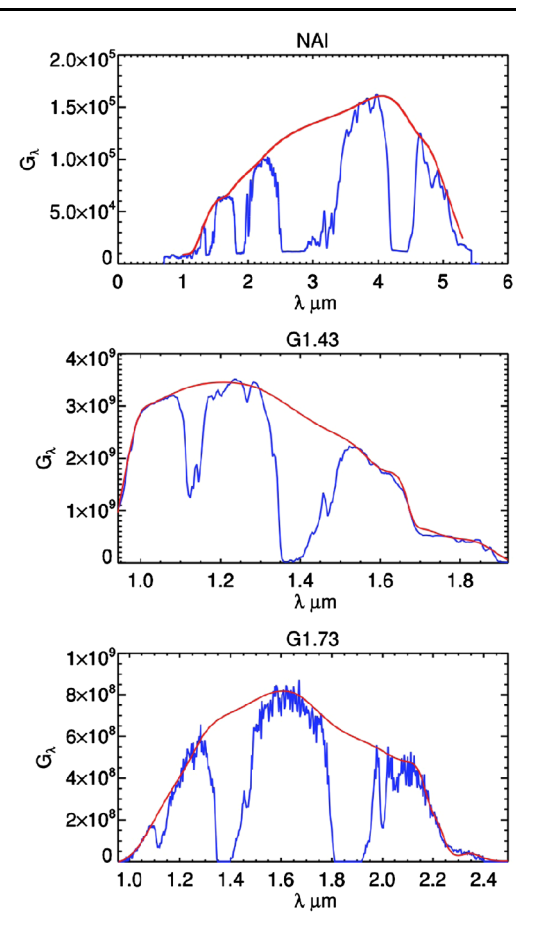
The relationship between counts C_{λ} , dark counts $D_{\lambda}(\tau)$ for exposure time τ , flux f_{λ} in units of total solar flux, and a linear gain term (G_{λ}) is assumed to be linear:

$$C_{\lambda} = D_{\lambda}(\tau) + G_{\lambda}(\tau) f_{\lambda} \tau. \tag{1}$$

Finally, the gain factor G_{λ} was determined from the observed count rates C_{λ} for those data when the disk was visible (such data we refer to as "Fcal" data, Judge *et al.*, 2019), and those for the dark frames. The top-most panel of Figure 7 shows the calibration curve $G_{\lambda}(\tau)$



Figure 7 Calibration curves are shown for the three ground-based infrared spectrographs. The *red curves* are used to calibrate the flux and hence intensity data. They are attempts by-eye to produce a smooth dependence of the gain, passing through the peak continuum counts on the detector, avoiding the telluric absorption bands. The exposure times were 2.5, 0.1 and 0.5 seconds, respectively.



we derived for the NAI spectrometer. The calibration curve applied to the data is the smooth curve marked in red. This curve was derived through a spline fit to an estimate of the spectrum as seen from above the Earth's atmosphere, in which visual estimates of the unattenuated spectrum were used to fill-in the attenuated regions, assuming the solar spectrum is continuous at low resolution.

The difference between the red and blue curves is assumed to be caused by telluric absorption in the well-known absorption bands seen in Figure 1 (see, *e.g.* Allen, 1973).

This procedure assumes that between the telluric bands the solar spectrum is dominated by the continuum – the spline fits are smooth functions. While this is a problem at blue and UV wavelengths, red and infrared solar spectra are not heavily line-blanketed. For example, between 2.25 and 14.3 microns, solar data from the ACE instrument on the SCISAT-1 spacecraft (Hase *et al.*, 2010) show that the average line absorption is just 0.9%. It has the advantage of using data close in time to the eclipse under varying thermal conditions. But this carries potential disadvantages of relying on uncontrollable conditions. Our resources were limited, some instruments were on temporary loan, and so we were unable to perform additional laboratory calibrations.

Theoretical wavelengths of lines of hydrogen are marked in black in the upper panel of Figure 1. Five lines of hydrogen and one of neutral magnesium were detected in emission, they are marked and identified in red. The detected hydrogen lines are those with the largest



transition probabilities and branching ratios between 1 and 5 microns, fully consistent with the spectrum expected from the chromosphere and/or prominences in this wavelength region.

Other "sharp" structures in the upper panel result from wavelength-dependent telluric absorption features, they are not solar emission lines. For reference, known wavelengths of coronal lines not seen with this instrument are marked, with their identifications in brackets. The identification of an emission line with a Mg I 5g-4f transition is based upon the fact that this has the largest angular momentum quantum numbers for a given principal quantum number. Such lines have branching ratios approaching one, and possess the largest cross section for population by recombination in prominence plasma.

There are several weak emission features between 3.969 and 3.986 μ m present in the NAI scans that we have been unable to identify. Three of these lie close to 3d-4p and 4p-4d transitions in C I, but the radiative branching ratios appear unfavorable, even if photon trapping in the stronger 2p-4d UV lines enhances intensities for two of these lines.

Below we will relate the NAI absorption and prominence spectra to the AIR-Spec data at full spectral resolution, addressing the motivations behind the work of Münch, Neugebauer, and McCammon (1967) and the present paper.

2.1.2. PolarCam Broad and Narrow-Band Polarization

HAO acquired and operated a 4D Technologies PolarCam 1920×1200 camera. The PolarCam is a bio-inspired polarization sensor based on the five polarization filtering micro-villi present in the compound eye of the mantis shrimp (York *et al.*, 2014). This novel CCD detector operates at speeds up to 30 frames per second with a micro-polarizer array placed over the sensor with four alternating orientations of linear polarizers. It was mounted at the focus of a Stellarvue D = 70 mm f/6 apochromatic refractor behind a filter wheel. The filter wheel contained two narrow-band filters to observe coronal emission at Fe X 637.8 nm and Fe XI 789.6 nm and a 46 nm wideband filter centered on 734.10 nm to observe the white-light continuum. Here we report on wideband data. The PolarCam pixel size is 2.87 arcseconds per pixel, yielding a spatial resolution of 5.74 arcseconds.

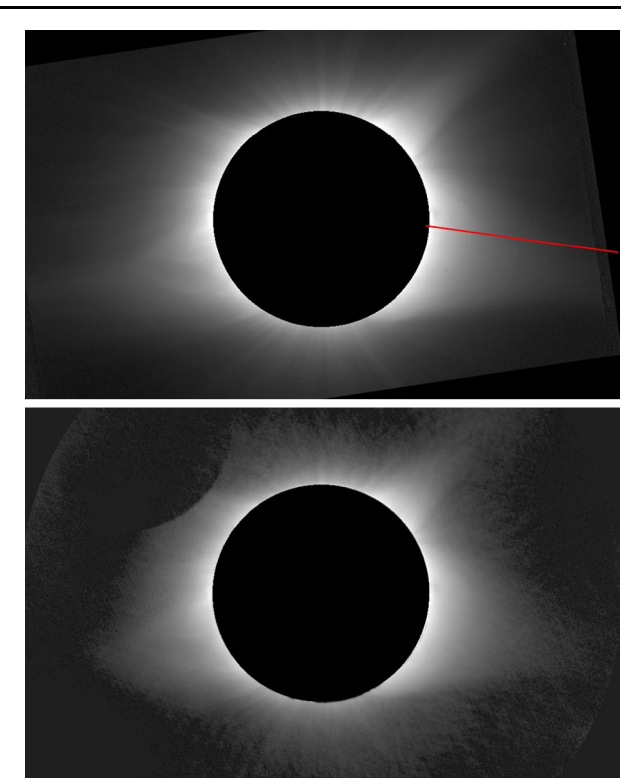
Continuum images were acquired at 60 msec exposure between 17:44:30 and 17:44:51 UT. The first few seconds of observations were not used because the filter wheel motion was settling. The remaining data were flat corrected and photometrically calibrated using an opal glass attenuator from the High Altitude Observatory set of fundamental standard opals. The linear polarization signal was constructed from a PolarCam superpixel that contains four individual pixels, each with a polarization acquired at one of four unique angles: 0, 45, 90 and 135 degrees. Images of the total coronal brightness and the polarization brightness (pB) were constructed from the four polarization states. Total intensity and pB images were integrated over 5 seconds of data between 17:44:38 and 17:44:43 to increase the signal-to-noise. The resulting PolarCam image of the calibrated pB is shown in the upper panel of Figure 8.

To estimate the accuracy of the calibrations, the PolarCam observations were compared with calibrated pB observations taken by the Mauna Loa COSMO *K-Coronagraph* (K-Cor) in Hawaii. K-Cor is an internally occulted white-light coronagraph that routinely views the pB of the solar corona over a field of view from 1.05 to 3 solar radii with 5.643 arcsecond pixels and a spatial resolution of 11.29 arcseconds. Circumstances of eclipse in Wyoming allowed us to acquire near-simultaneous K-Cor data with PolarCam. A K-Cor pB image taken at 17:44 UT is shown in the lower panel of Figure 8. The K-Cor and PolarCam pB images are shown using the same intensity scaling and color table, and to enable a direct



Eclipse Observations Page 11 of 23 **166**

Figure 8 Top panel: PolarCam calibrated polarization brightness image of the total solar eclipse on 21 August, 2017 averaged over 5 seconds between 17:44:38 and 17:44:43 UT. The red line denotes the location of 265 degrees position angle displayed in the scan in Figure 9. Solar north is straight up. Bottom panel: An image of the white-light polarization brightness (pB) corona obtained at 17:44 UT on 21 August, 2017 by the K-Cor instrument on Mauna Loa.

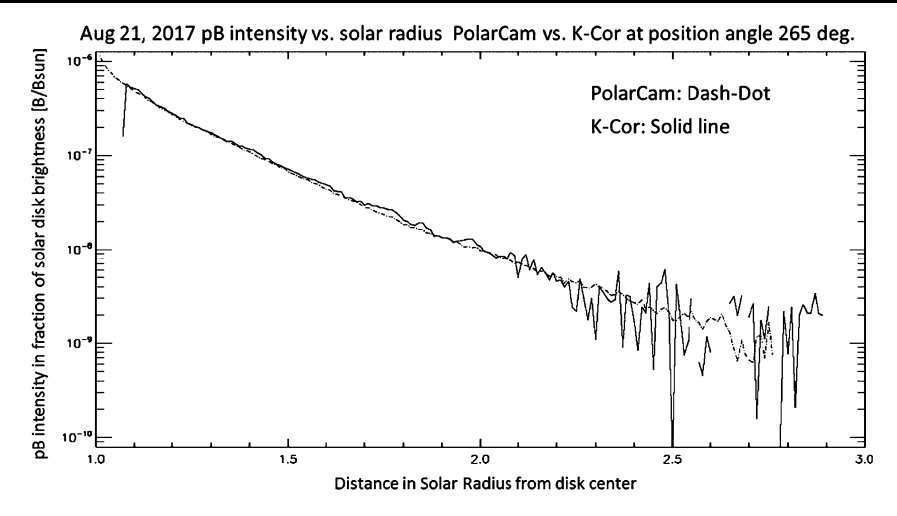


comparison, the PolarCam image has been reduced in size to match the spatial scale of the K-Cor image. The K-Cor instrument has an internal occulter that blocks the lower corona out to 1.08 solar radii. The Moon is visible in the upper left of the K-Cor image. In the figure, the PolarCam data have been masked below 1.08 solar radii, even though the Moon extended over just 1.013 solar radii in the original PolarCam image.

Clearly, the two images are qualitatively a good match. A more quantitative comparison is shown in the line plots of Figure 9. The upper panel compares the calibrated pB as a function of height, along the red line in Figure 8, a position angle of 265 degrees. The lower panel compares the pB at data as a function of all position angles, at a height of 1.35 solar radii. The datasets are in overall good agreement. The K-Cor instrument views the corona through a much brighter sky and hence entails removal of a significantly noisier background. Sky brightness during a total solar eclipse is about a thousand times darker than coronal skies at good coronal sites such as Mauna Loa. Total solar eclipses provide the conditions needed to view the unpolarized white-light corona from the ground and to record the polarized corona with significantly greater signal-to-noise than can be achieved by ground-based internally occulted coronagraphs. The Mauna Loa skies during the eclipse were noisy but good enough to obtain some K-Cor observations. The noise in the K-Cor data on this day was $\approx 3 \times 10^{-9} B/B_{\odot}$, $(B/B_{\odot}$ denotes brightness with respect to the solar disk) as can be seen in the upper panel of Figure 9. Results from this preliminary work show that the PolarCam demonstrated the ability to acquire high quality polarization images with no instrumental polarization optics, which has significant benefits for space-based observations. A more complete analysis of the data acquired by PolarCam experiment will be presented in an upcoming paper.



166 Page 12 of 23 P. Judge *et al.*



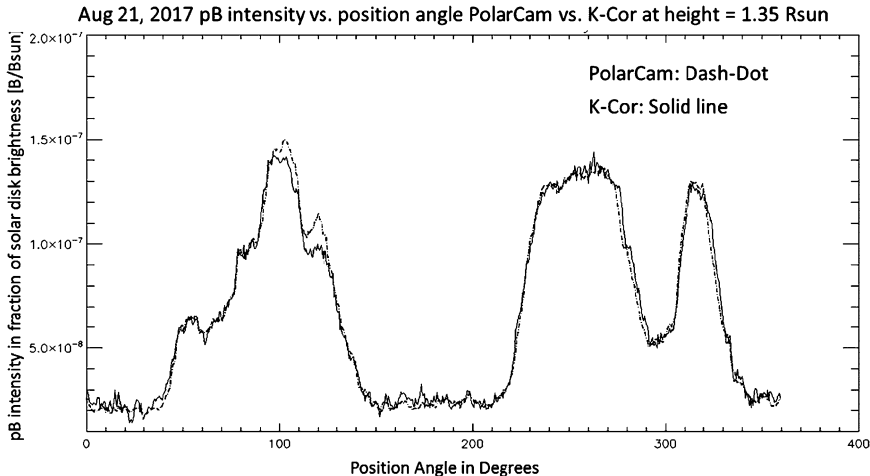


Figure 9 *Upper panel*: Radial scan of calibrated pB intensity from PolarCam and K-Cor at 265 degrees position angle, as indicated by the *red line* the Figure 8. The two datasets show good overall agreement of calibrated pB intensities as a function of height out to 2.2 solar radii. Beyond 2.2 solar radii the sky background overwhelms the K-Cor coronal signal. *Lower panel*: Azimuthal scan of calibrated pB intensity from PolarCam and K-Cor at the height of 1.35 solar radii. There is good overall agreement between the two datasets on a pixel-to-pixel basis.

2.1.3. Avantes Spectrographs

Three low-resolution spectrographs were kindly loaned to us by the Avantes corporation. Their primary characteristics are listed in Table 2, for more details see Judge *et al.* (2019). Each instrument was fed by light from a pupil plane, by optical fibers. Thus each spectrum is the integrated flux from the entire field of view of each instrument. The calibrations are described by Judge *et al.* (2019), based upon the models for the brightness of the crescents as a function of time (see Figure 5), using limb darkening at the central wavelength (or nearby wavelengths when telluric absorption is too strong). Infrared spectra from the NAI and Avantes spectrometers are shown in the lower panel of Figure 1, normalized to disk-center intensity and at roughly the same spectral resolution. The spectra show the same



Eclipse Observations Page 13 of 23 166

Table 2 Experiment details.

Name	Field of view	Nominal λ range (μm)	Δλ (nm)	Notes
AIR-Spec	$10'' \times 1.55R_{\odot}$	2.84 – 3.08, 3.74 – 3.98	0.2	1st order
•	· ·	1.42 – 1.54, 1.87 – 1.99	0.1	2nd order
 Slitjaw cam. 	$\approx 2.6R_{\odot} \times 2.3R_{\odot}$			
NAI	disk of $3R_{\odot}$ radius	1800-14,000* cm ⁻¹ (0.715-5.555 μm)	0.0904* cm ⁻¹	
Avantes G0.70	100"-wide slot	0.296 - 1.100	0.6 - 0.55	afocal
G1.43	disk of $2R_{\odot}$ radius	0.942 - 1.924	4.15 - 3.35	//
G1.73	disk of $2R_{\odot}$ radius	0.954 - 2.500	3.2	″
PolarCam	$\approx 5R_{\odot} \times 4R_{\odot}$	0.637,0.789, 0.734	1,1,50	
FLIR/Madras	$\approx 3.4R_{\odot} \times 1.7R_{\odot}$	3.95 [Si IX]	39	

The solar radius seen from Earth is 948.7". All observations were centered around local mid-eclipse times, close to 17:21 UT at Madras OR, 17:44 UT at Camp Wyoba, and 18:24 UT for AIR-Spec on board the G V aircraft. *Data are wavenumbers ($\tilde{\nu}$), the spectral resolution is constant in wavenumbers.

absorption features from the Earth's atmosphere. The chromospheric and coronal data from the Avantes instruments are analyzed in more detail by Judge *et al.* (2019). No coronal line emission was detected from the ground, consistent with the estimated instrumental sensitivities (see Figure 4).

Light fed to the G0.70 spectrograph was limited by inclusion of a field stop at prime focus as indicated in Figure 2. The light was admitted through the two rectangular blue boxes shown, at C2 and C3. The G0.70 spectra are therefore from a restricted (100"-wide) arc of all the emission from above the lunar limbs. It happened to exclude the prominence from the light feed at the west limb. Only telescope jitter and seeing-induced image motions in the direction tangential to the limb can affect the flux measurements. Previous eclipses suggested that seeing is at worst 5", which means that the 100" wide slot probably contains some small seeing-induced residual signals, as any excursions tangential to the limb sampled statistically similar regions of the limb atmosphere. Figure 7 shows the calibration curves for the G1.43 and G1.73 spectrographs. Unlike the curve for the G0.70 spectrograph shown in the paper by Judge *et al.* (2019), there is no "UV enhanced" bump in gain curves at the shortest wavelengths.

The Avantes spectra, including those from the visible spectrometer, are analyzed in detail by Judge *et al.* (2019). Two emission lines were not identifiable. They appeared most clearly near 5–10 seconds before third contact. These lie close to 369.5 and 660.9 (330.5 in second order perhaps) \pm 0.3 nm.

2.2. At Madras, Oregon

One of us (A.R.) fielded an infrared FLIR camera from Madras, Oregon (Longitude W 121° 07′ 46.0″, Latitude N 44° 38′ 0.0″, altitude 683 m). Second contact at Madras was at 17:19:36, third at 17:21:38 UT. A FLIR SC8300 Thermal Imaging Camera with a focal length of 1152 mm was used, along with a SPECTROGON narrow-band filter centered at 3.964 μ m, with a FWHM 0.04 μ m, and a near-Gaussian profile between 3.9 and 4.0 μ m. The filter width is 100 times larger than the expected width of the [Si IX] coronal line, and the transmission of the filter is 20% at the center of the line. The NAI photospheric spectra reveal atmospheric transmissions across the peak of the filter that are close to unity. As a



166 Page 14 of 23 P. Judge *et al.*

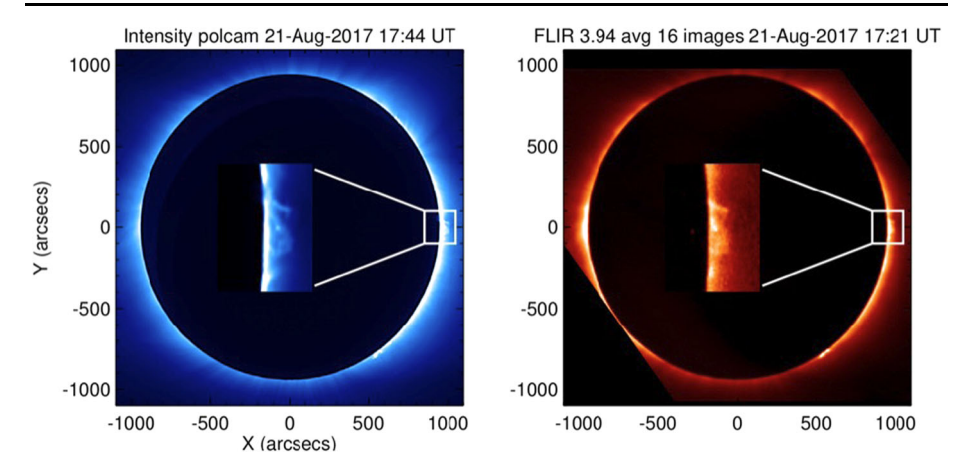


Figure 10 The *left panel* shows PolarCam broadband ("white-light") intensities near 734 nm, the *right* shows a sum of 16 FLIR images close to $3.96 \, \mu m$, obtained by Richards at Madras, Oregon. The latter were acquired through a $3.96 \, \mu m$ filter, with a FWHM of $0.04 \, \mu m$. This bandpass is dominated by continuum, not line emission. The *insets* show detailed structure of the region in the square. The FLIR inset is the sharpest of the images from that camera. Notice the similarity of structures on all scales in both panels.

result, the K-corona continuum contributed 500 times as many photons for the same peak line intensity as the continuum.

The FLIR InSb sensor has a 1344×784 format and a detector pitch of $14 \mu m$. The full field of view was 3280×1650 arcsec. Figure 10 shows the resulting narrow-band image of the corona, along with a white-light intensity data from PolarCam. Both images have been rotated so that solar N is along the positive y-axis, W along +x.

The similarity between the images shows that the FLIR data are dominated by emission from the K-corona. A filter some ten times narrower with a peak close to the rest wavelength of [Si IX] would be needed for the line to contribute equally to the continuum. Even though we could not detect [Si IX] 3.935 μ m line emission, it is significant and encouraging that a commercial camera in which only the sensor was cooled was able to obtain such clean data as far as 3.96 μ m into the infrared.

2.3. AIR-Spec on the NCAR Gulfstream V Aircraft

The AIR-Spec instrument consists of an image stabilization system, telescope, infrared spectrometer, and visible slit-jaw imager. The image stabilization system includes a set of fiberoptic gyroscopes to measure aircraft motion and a fast-steering mirror to redirect the line-of-sight. The stabilized beam is collected by the telescope, which focuses it onto a mirrored slit-jaw. Visible light reflected by the slit-jaw is imaged by the slit-jaw camera, while infrared light passing through the slit is dispersed by a diffraction grating and focused onto an infrared detector. In order to minimize the thermal instrument background and dark current, the spectrometer optics are housed in a vacuum chamber and cooled to below 150 K with liquid nitrogen, the infrared camera interface is packed in dry ice, and the infrared detector is cooled to 59 K by a closed-cycle cryogenic cooler.

The spectrometer measures first and second order light in two passbands centered on 2.9 (1.45) and 3.9 (1.95) microns. The width of each passband is about 2400 Å in first order and 1200 Å in second order. The linear dispersion is 2.4 Å/pixel in first order and 1.2 Å/pixel in second order. The spatial sampling is 2.3 arcsec/pixel and the field of view is 0.4 degrees.



Table 3	AIR-Spec	slit positions.
Table 5	AIK-Spec	SHE DOSILIONS.

Slit Position	Duration	IR Frames	SJ Frames
1. West limb	63.5 sec	953	2083
2. Prominence	41.5 sec	622	1359
3. East limb	35.7 sec	536	1171
4. Prom. & west limb	82.4 sec	1236	2702
5. Chromosphere	5.1 sec	77	168

Figure 11 Summary of the AIR-Spec eclipse observations. The average spectrum at the limb is shown in blue (3 micron channel) and red (4 micron channel) for each slit position. The first and second-order continua and dark background have been subtracted. Four of the five target lines appear in the coronal positions, and hydrogen appears in the prominence and chromosphere. Superscripts in parentheses indicate whether each line is measured in first or second order.

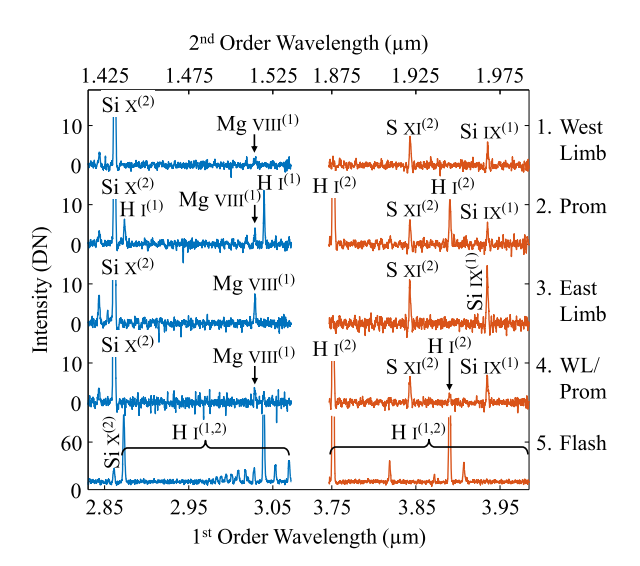


Table 4 Measured wavelengths for the AIR-Spec coronal lines.

	Si x	S XI	Mg VIII	Si IX
1.	$14308.3 \pm 0.5 \text{ Å}$	$19214.0 \pm 0.4 \text{ Å}$	$30285.8 \pm 1.5 \text{ Å}$	$39349.8 \pm 0.9 \text{Å}$
2.	$14308.3 \pm 0.5 \text{ Å}$	$19213.8 \pm 0.5 \text{ Å}$	$30282.8 \pm 1.1 \text{ Å}$	$39349.8 \pm 0.9 \text{ Å}$
3.	$14308.0 \pm 0.5 \text{ Å}$	$19214.1 \pm 0.4 \text{ Å}$	$30286.4 \pm 0.9 \text{ Å}$	$39349.7 \pm 0.9 \text{ Å}$
4.	$14308.4 \pm 0.5 \text{ Å}$	$19214.9 \pm 0.4 \text{ Å}$	$30285.3 \pm 1.2 \text{ Å}$	$39349.4 \pm 0.9 \text{ Å}$
	$14308.3 \pm 0.3 \text{ Å}$	$19214.2 \pm 0.2 \text{ Å}$	$30285.1 \pm 0.6 \text{ Å}$	$39349.7 \pm 0.5 \text{ Å}$

Wavelength estimates and standard errors are reported for each of the four coronal slit positions. The *last row* contains the mean wavelength of each line across all four positions, along with its uncertainty. All wavelengths are given in vacuo.

AIR-Spec viewed the total eclipse between 18:22 and 18:26 UTC from 14.3 km above western Kentucky. During totality, the instrument took observations in three coronal locations: east and west coronal streamers and through the western prominence (Figure 2, Table 3). The coronal data have 60 ms exposure time, dictated by the thermal background, and a 15 Hz cadence. Chromospheric spectra (30 ms exposure time) were taken during 3rd contact.

Figure 11 shows the average spectrum at each slit position over the 35 arcseconds (15 pixels) nearest to the lunar limb. Four of the five targeted coronal lines are seen in each



166 Page 16 of 23 P. Judge *et al.*

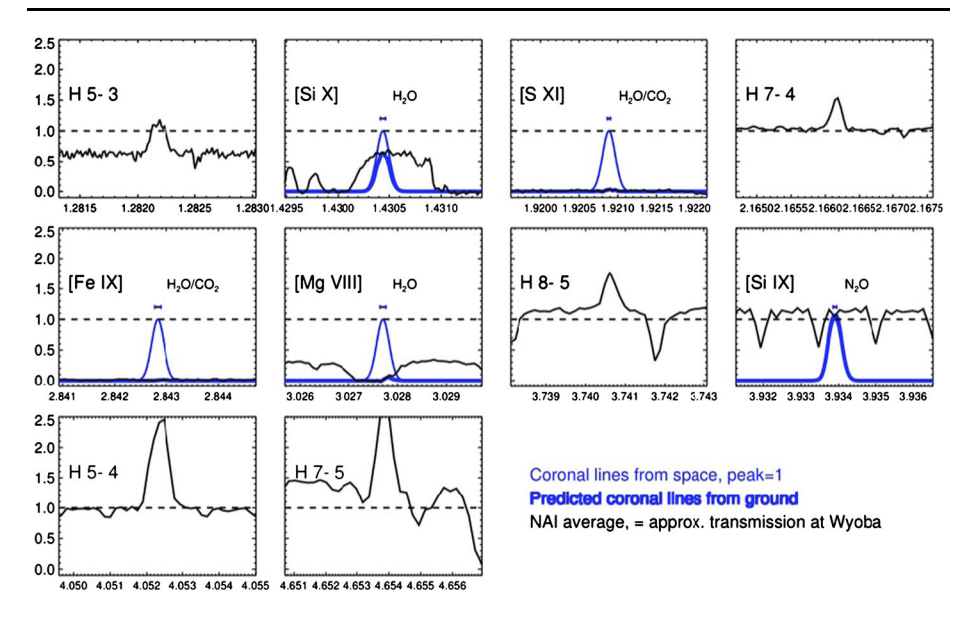


Figure 12 The figure shows measured NAI spectra in *black*, in units of the flux from the integrated solar disk, of the solar photosphere and chromosphere. A value close to 1 indicates 100% transmission of the atmosphere, at Camp Wyoba on the day of the eclipse. *Thin blue lines* show the expected profile of coronal lines, with a peak value at unity. The wavelengths are those measured by the AIR-Spec experiment, and the error bars show the uncertainties in AIR-Spec wavelengths. *Dark blue lines* show the product of the NAI and coronal profiles, representing approximately the flux profiles measured on the ground under conditions prevalent at Camp Wyoba. Also shown are NAI profiles at the wavelengths of several hydrogen lines. Wavelengths are in air.

of the coronal positions, with measured wavelengths reported in Table 4. In the prominence and during the 3rd contact flash spectra, strong H I lines are seen. We have not confirmed detection of the fifth target coronal line, Fe IX at 2.85 µm, but a weak feature on the east limb appears at that wavelength. We will re-assess this detection after AIR-Spec observes the 2019 eclipse over Chilean airspace, with increased sensitivity. A feature at 2.84 µm previously thought to be Fe IX is now known to arise from stray reflections inside the spectrometer (Samra *et al.*, 2019, erratum).

3. The Solar Spectrum

3.1. Emission Lines in Relation to Telluric Absorbers

Figure 1 shows the average fluxes of all the scans measured by the NAI instrument before second contact. The figure documents known emitters and telluric absorbers at a low spectral resolution. In the lower panel, the NAI data are compared with the "Fcal" data obtained on the solar disk with the Avantes IR instruments (see Judge *et al.*, 2019). Where the wavelengths overlap (below 2.2 µm), the agreement between the smoothed NAI data and Avantes spectra shows that our independent flux calibrations are better than 13%.

The full resolution NAI data shed light on the observability of emission lines with, for example, DKIST. Figure 12 shows the NAI photospheric measurements on a scale where the photospheric brightness is one. The panel labeled "H 5-3", for example, shows the overall



Eclipse Observations Page 17 of 23 166

transmission is close to 0.6 at this particular wavelength. In contrast, the "H 7-4" and "H 5-4" transitions lie in a region where the transmission is one, and these lines of hydrogen lie above the continuum measured by NAI during the approach to C2.

Superposed on the NAI spectra are shown in blue typical emission profiles centered precisely at wavelengths determined with AIR-Spec, of the coronal emission lines detected, including error bars on the central wavelengths. The emission lines are shown with Gaussian profiles with a full-width at half-maximum (FWHM) of 30 km s⁻¹ in Doppler units. This is a typical value for forbidden lines from the corona (Billings, 1966). The dashed line marks a transmission level of 1, for comparison with the Gaussian profiles of coronal lines seen above the atmosphere (thin blue line) and what might be expected at Camp Wyoba (thick blue line).

The consequences of these results for the future of coronal polarimetry are mixed. The good news is that the 3.935 μ m line of [Si IX] lies in a region only moderately disturbed by telluric attenuation. Either side of the line, plenty of "continuum" pixels are available where the continuum is flat, lying between the well-documented absorption lines of N₂O. Large variable backgrounds due to changing transmission and emission from scattering in the Earth's atmosphere present the greatest challenge to sensitive measurements of the coronal magnetic field using such lines (*e.g.* Judge *et al.*, 2001). Thus, [Si IX], along with the two well-known lines of [Fe XIII] at 1.0747 and 1.0798 μ m and the 1.43 μ m line of [Si X] remain the best candidates for polarimetry (Judge *et al.*, 2001, 2002; Penn *et al.*, 2004). Some less good news involves the line of [Mg VIII], which is attenuated by significant non-flat profile of H₂O absorption (see the difference between the un-attenuated blue curve and the thick blue curve in the panel labeled "[Mg VIII]" in Figure 12). On balance, it seems fortunate that the [Si IX] and [Si X] lines at will offer new opportunities with the DKIST, even if the [Mg VIII] line will present challenges because of significant telluric absorption.

3.2. Persistent He 1083 nm Emission During Totality

The permitted transitions of He I at 1.083 µm struck us as being, in essence, both chromospheric—showing a steep dropoff with time after C2 and a steep increase before C3—and coronal—showing persistent emission 92 seconds before C3. Figure 13 compares the behavior of helium and hydrogen lines during totality. Clearly the emission close to 1.083 µm extends deep into totality, unlike the line of hydrogen which is measurable only within 15 seconds or so near C2 and C3. In the upper panel, we show wavelengths of lines of He I and Fe XIII at 1074.7 and 1079.8 µm along with the Avantes spectra. The wavelength scale of the Avantes data was checked against the NAI data, and found to be accurate to about 1/10 of a wavelength pixel, or 0.4 nm. In the corona, the 1074.7 nm line is on average some 2-3 times brighter than that at 1079.8 nm (Judge, 1998). Clearly the emission detected is entirely due to helium. But it should be noted that the profile of the 1.083 µm emission is peculiar, a surprising result given the low resolution of the G0.70 spectrometer. Figure 13 reveals that the emission decreases slowly from the center of the line to the short-wavelength side but decreases very sharply on the long wavelength side. Unfortunately, the same is true for the 1.280 μ m emission of H I, present only when close to C2 and C3 (t = 0 in Figure 13). The short-wavelength emission extends some 4 pixels to the short-wavelength side of the line, some 13 nm in wavelength, to 1070 nm, a Doppler blue-shift of 3600 km s⁻¹. These peculiar profiles, lead us to suspect instrumental origins for these peculiar profiles, and not emission at the [Fe XIII] wavelengths at 1074.7 or 1079.8 nm. The NAI scan obtained 4 seconds before C2 shows the presence of the two He I components but no hint of signals of [Fe XIII] or other emission extending 15 nm shortward of 1083 nm. It must be noted that the NAI instrument lacks sensitivity at these short wavelengths (Figure 7).



166 Page 18 of 23 P. Judge *et al.*

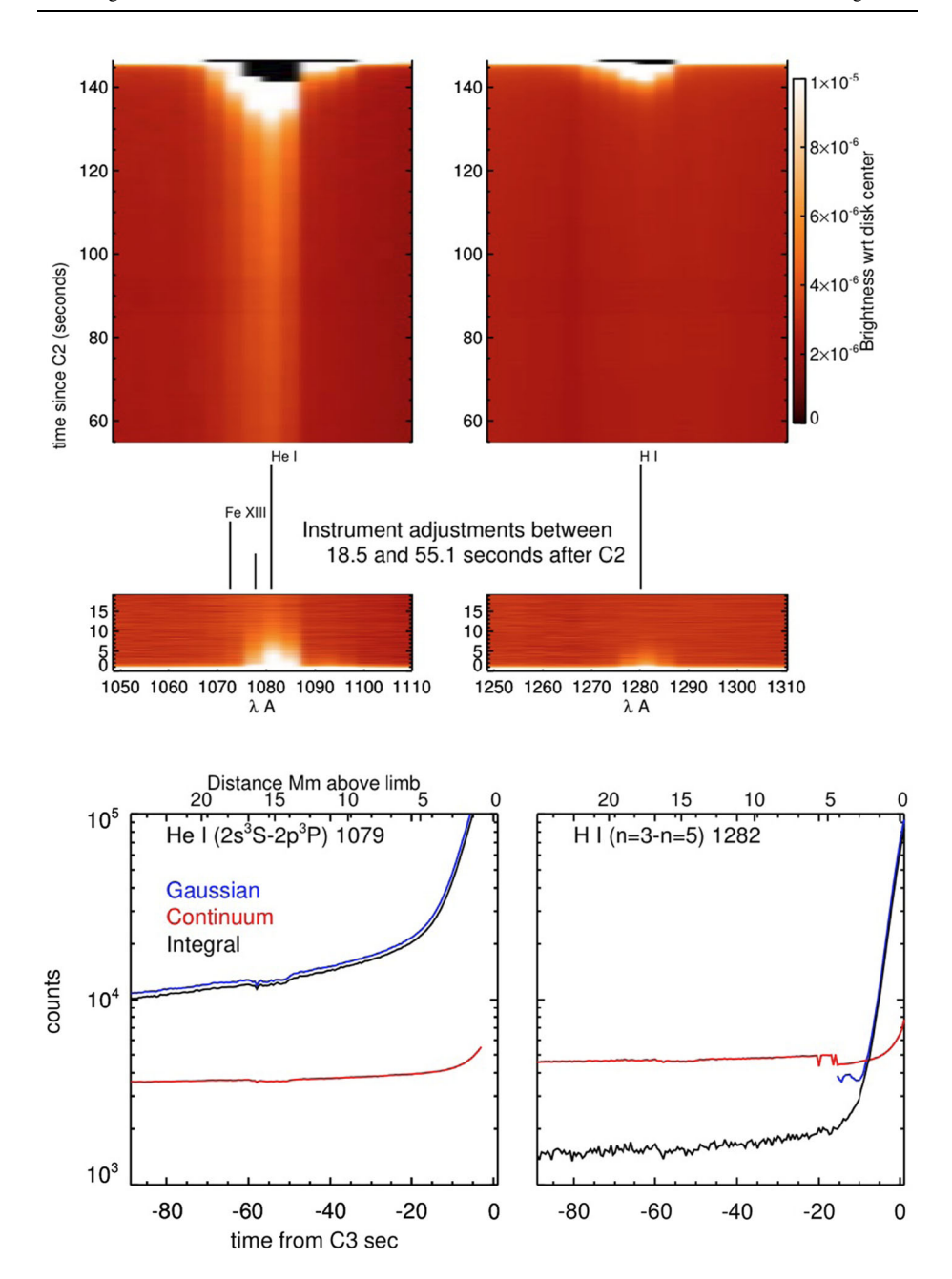
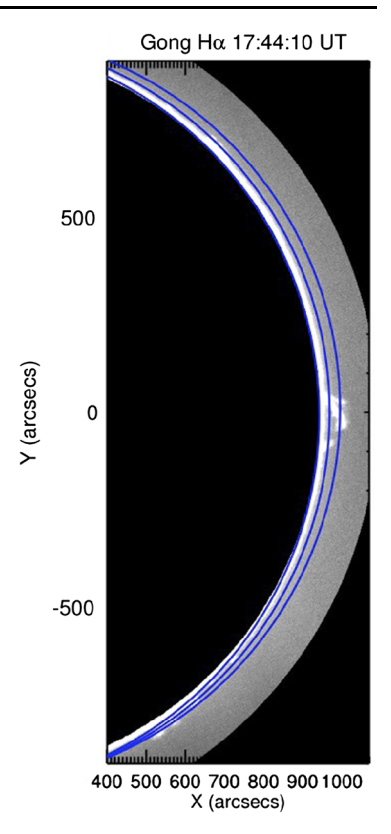


Figure 13 *Upper (image) panels*: intensities relative to disk center are shown as a function of wavelength vs. time from second to third contact, from the G1.43 spectrograph. The conversion from flux to intensity uses solid angles for the continuum corona (section 2.4 of Judge *et al.*, 2019). This calibration over-estimates the intensity of the He I line (see text). Data were not acquired in the gap between 18.5 and 55.1 seconds after C2. Saturated pixels in the core of the He I line are marked in black. *Lower panels*: Wavelength-integrated counts for the He I 1083 nm and H I n = 3 - n = 5 transitions are shown as a function of time from third contact, as measured from the 500 msec exposures.



Eclipse Observations Page 19 of 23 **166**

Figure 14 The image displays GONG Hα data close to mid-eclipse, on the western solar limb. The *blue lines* show the lunar limb computed at mid eclipse, and second and third contact. The prominence material seen close to one, three and five o'clock is almost completely covered at C2, and is gradually more visible to afocal instruments as the eclipse proceeds. No prominence was visible on the solar east limb in the GONG data.



Yet the helium multiplet remains bright in the G1.43 spectra, significantly above the neighboring continuum for all scans. Figure 14 shows the brightness of the H α emission line at the west solar limb obtained close to mid eclipse, by the GONG project. Three groups of prominences were present on the W limb. If these prominences dominated the emission in He I 1083 nm, then the emission would steadily increase throughout the period C2-C3, contrary to the observed behavior (Figure 13).

Thus the question arises as to the origin of the 1.083 µm emission throughout the eclipse. The emission is not at the correct wavelength to be attributable to [Fe XIII], and the emission is simply too bright to be from a coronal emission line. The very slow rise from −90 to −20 seconds before C3 suggests that it is not related to the prominences that are present on the W. limb. While they certainly contribute, they should also contribute to the H I line emission similarly, in contrast with the upper and lower plots of Figure 13. We therefore suggest instead that the 1.083 µm emission does not arise mostly from a prominence source. Instead, it appears to be emission from cool regions distributed within the corona. Such emission has been reported by Kuhn and colleagues during and outside of eclipses over several decades (see, e.g. Moise, Raymond, and Kuhn, 2010). As well as implications discussed in the work of Kuhn and colleagues, the presence of extended neutral helium emission suggests that ion-neutral collisions might be responsible for converting ordered (Alfvén-like) motions into heat, providing the needed natural dissipation mechanism for heating the diffuse solar corona (e.g. Zaitsev and Shibasaki, 2005).

The physical intensities of the 1.082 μ m emission are in fact in rough agreement with those measured by Kuhn, Penn, and Mann (1996), varying from 5×10^{-7} to 3×10^{-7} be-



166 Page 20 of 23 P. Judge *et al.*

tween 1 and $2R_{\odot}$. The reason the counts are so large is seen from both panels of Figure 3 of Kuhn, Penn, and Mann (1996): the diffuse helium emission drops very slowly with heliocentric distance. The G1.43 experiment integrated all emission within a radius of $2R_{\odot}$. The solid angles for integration of intensity to derive flux (and counts) for 1083 and 1074.7 are then 3π and 0.6 in units of R_{\odot}^2/d^2 where d=1 AU. We find that the average He and Fe intensities are 7×10^{-7} and $< 10^{-6}$ in units of B_{\odot} , respectively, over these solid angles.

Ding and Habbal (June 2018, private communication) reported highly Doppler-shifted components to He 1083 on the blue side. But we noted that mission out to 1.07 μ m requires blue-shifts of 3600 km s⁻¹. In an abstract, Habbal *et al.* (2018) report extended emission perhaps compatible with our finding of emission throughout totality, noting

...cool prominence material at less than 10,000 to 50,000 K, within more than a radius above the solar surface...

Further sensitive spectral experiments during eclipse seem warranted, including perhaps observations of the D₃ line at 587.6 nm.

3.3. The Afocal Experiments

Our decision to obtain data afocally was initially made to explore how spectrographs might be used as spectro-photometers, sampled very rapidly in time. Our initial idea was to attempt to invert profiles of bright chromospheric lines obtained as a function of time, to reveal the changing profiles as a function of height above the solar photosphere. The resolution achieved in principle can approach $2\tau v_{\text{Moon}}$ where $v_{\text{Moon}} = 280 \text{ km s}^{-1}$ is the speed of the lunar limb across the solar disk as projected on the Sun. For a 10 msec exposure, this resolution is 5.6 km, compared with a stratified chromospheric depth of 2000 km and spicules of typical length 4000-8000 km. The afocal approach also avoided careful focusing and led us to avoid highly precise pointing, while at the same time allowing high relative photometric precision under conditions of transparent skies.

Spicules have always been assumed to comprise an important component of the physical connection between the lower atmosphere and corona. For over a century, they were assumed to be jet-like chromospheric features extending from the chromosphere into the corona. In 2007, space-based data of the central 3 Å of the Ca II H line, from the Broadband Filter Instrument (BFI) on the Hinode spacecraft, were obtained with sufficient stability, cadence and angular resolution, to see in greater detail the nature of these phenomena. The results were documented by de Pontieu et al. (2007). The spicules were classified into two types, but neither were related to the earlier literature. Again these phenomena were interpreted in terms of tube-like structures. Beginning in 2010, Judge and colleagues have proven that at least one type of disk-counterpart cannot be of a tube-like form, and instead at least some of the dynamic changes seen above the limb are more likely projections of current sheets pervading the low plasma β atmosphere (Judge, Tritschler, and Low, 2011; Judge, Reardon, and Cauzzi, 2012; Lipartito et al., 2014). This debate is not settled, although inspecting rate of citations of the two pictures in the literature, the "tube" hypothesis seems to be favored by many.

The *Hinode* BFI instrument integrates spectra over 3 Å. This includes the 0.5Å-wide chromospheric Ca II H line core, but on the disk the signals are dominated by the bright inner wings formed in the upper photosphere. The consequences were highlighted by Judge and Carlsson (2010). They argued that the peculiar lack of a stratified layer between the



Eclipse Observations Page 21 of 23 166

photosphere and corona, in the *Hinode* data, must be due to the tendency of wavelength-integrated lines to appear to emerge directly out of the photosphere. For completeness, we note that emission from the (cool) CO molecule extends above the solar limb (Ayres and Rabin, 1996), but that it has a small scale height that would yield a very sharp drop after second contact and a sharp rise just before third, lasting a couple of seconds. It therefore has no significant relationship with the detected helium emission.

The spectral sampling of the G0.70 spectrograph is 5.5 Å, roughly twice the width of *Hinode*'s BFI. Further, the data quality were not sufficient to achieve a time resolution even close to 5.6 km. Atmospheric seeing in the direction tangent to the limb will only increase the noise, and the telescope apertures used were small. But the Avantes data illustrate that such experiments can, and perhaps should be done in the future, to explore what can be learned using the full limb emission coupled with larger telescopes and a higher-resolution spectrometer.

3.4. The Need for a Coronal Spectral Survey

Samra *et al.* (2018) discovered an unidentified line, close to the line of [Fe IX] at 2.85 µm. The sensitivity of AIR-Spec exceeded that of the NAI by a factor of 50 or so. Yet, AIR-Spec sampled very little of the infrared spectrum. It is therefore possible that unanticipated lines of the corona exist but which we have not yet been able to detect. The NAI, or another instrument, would greatly benefit from a high-altitude flight, fed with a photon-capturing telescope to improve signal-to-noise ratios. Samra and colleagues flew an improved AIR-Spec instrument during the 2nd July 2019 eclipse over Chilean airspace. Preliminary analysis indicates significant improvement in the data quality over those from the eclipse reported here.

At first light (2020), the DKIST will observe particular regions of the infrared spectrum out to 5 μ m using the Cryo-NIRSP instrument. Yet, we have no measurements of the coronal spectrum across the mid IR region (2–5 μ m). It seems advisable to obtain an FTS spectrum of the corona from above the atmosphere, which can be readily compared with the transmission measurements made during this 2017 eclipse campaign with the NAI.

4. Conclusions

We successfully deployed five of six experiments at Camp Wyoba, four of which obtained spectra afocally, integrating light from around the lunar disk with little or no information on the location of such emission. One of us (A.R.) successfully acquired narrow-band images centered near 3.96 µm, revealing spatial distributions of brightness obviously the same as white-light intensity images, with a commercial IR camera. The high cadence and visibleinfrared wavelength coverage of our measurements were unique. The ground-based data were successfully, if sometimes crudely, reduced, successful in the sense that the data were mutually consistent, consistent with theoretical expectations and the accompanying aircraft experiment obtained as part of our campaign (more details can be found in the thesis of Samra, 2018). Our unique ground- and aircraft-based campaign has enabled us to assess the likely viability of various infrared lines for coronal magnetometry, for example using the DKIST facility. It has revealed curious neutral helium emission throughout totality that appears to originate in the corona (and not chromosphere or prominences). Perhaps most significantly, we have demonstrated (1) the power of using afocal spectro-photometry as a new tool for probing long-standing problems in the solar atmosphere, such as the physical properties of the chromosphere and enigmatic spicules, and (2) that the [Si IX] 3.9346 µm line will be of great importance for magnetometry of the corona in the future.



166 Page 22 of 23 P. Judge *et al.*

5. Contributions

B. Berkey, A. Boll, P. Bryans, K. Gibson, and S. Tomczyk worked on the experiments fielded at Camp Wyoba. S. Tomczyk, J. Burkepile and G. de Toma processed and analyzed the PolarCam data. P. Cheimets, E.E. DeLuca, J. Samra and V. Marquez flew on the G V aircraft and obtained the AIR-Spec data. The AIR-Spec instrument was developed by the CfA team including also C. Madsen, L. Golub and A. Vira. The NAI experiment was designed and constructed by J.W. Hannigan with the assistance of S. Sewell, both of whom ran the instrument at Wyoba. A. Boll developed control software and ran the PolarCam instrument. A. Richards performed the experiment and reduced the data for the successful FLIR experiment at Madras, OR. P.G. Judge conceived the idea of the campaign, wrote a proposal for use of the HIAPER aircraft, and drafted early versions of the paper.

Acknowledgements We gratefully acknowledge HAO director Scott McIntosh and NASA-ISE (P. Bryans PI) supported the NAI experiment; Vanda Grubisic and her team at the EOL-NCAR laboratory for support during planning, proposing for and flying the G V aircraft; the NSF MRI program and the Smithsonian Institution for supporting the AIR-Spec project through grant AGS-1531549; NASA-ISE for support of the ROSETTA STONE proposal (P. Judge and S. Tomczyk PIs) funding the ground-based FLIR and PolarCam instruments; FLIR for the generous loan of their infrared camera; Avantes corporation for the generous loan of three spectrometers between 0.31 and 2.5 microns; NSF's REU program for support of A. Boll, K. Gibson and A. Vira. We thank the people at Camp Wyoba for their generous hospitality, enthusiasm and kindness.

Disclosure of Potential Conflicts of Interest The authors declare that they have no conflicts of interest.

Publisher's Note Springer Nature remains neutral with regard to jurisdictional claims in published maps and institutional affiliations.

References

Allen, C.W.: 1973, Astrophysical quantities, Athlone Press, London.

Ayres, T.R., Rabin, D.: 1996, Astrophys. J. 460, 1042. DOI.

Billings, D.E.: 1966, A guide to the solar corona, Academic Press, New York.

Casini, R., White, S.M., Judge, P.G.: 2017, Space Sci. Rev. 210, 145. DOI.

Coffey, M.T., Hannigan, J.W., Goldman, A.: 2006, J. Geophys. Res., Atmos. 111. DOI.

De Mazière, M., Thompson, A.M., Kurylo, M.J., Wild, J.D., Bernhard, G., Blumenstock, T., et al.: 2018, Atmos. Chem. Phys. 18, 4935. DOI.

de Pontieu, B., McIntosh, S., Hansteen, V.H., et al.: 2007, Publ. Astron. Soc. Japan 59, 655. DOI.

Del Zanna, G., DeLuca, E.E.: 2018, Astrophys. J. 852, 52. DOI.

Eddy, J.A.: 2009, The Sun, the Earth and Near-Earth Space: A Guide to the Sun-Earth System (NASA).

Golub, L., Pasachoff, J.M.: 2009, *The Solar Corona*, 2nd edn. Cambridge University Press, Cambridge.

Grotrian, W.: 1933, Z. Astrophys. 7, 26.

Habbal, S.R., Ding, A., Druckmuller, M., Solar Wind Sherpas: 2018, In: Observations of the Dynamics and Thermodynamics of the Corona during the 21 August 2017 Total Solar Eclipse, American Astronomical Society Meeting Abstracts 231, 220.07.

Hase, F., Wallace, L., McLeod, S.D., Harrison, J.J., Bernath, P.F.: 2010, J. Quant. Spectrosc. Radiat. Transf. 111, 521.

Hoyle, F.: 1955, Frontiers of Astronomy, Heinemann Educational Books, London.

Judge, P., Casini, R., Tomczyk, S., Edwards, D.P., Francis, E.: 2001, Coronal Magnetogmetry: A feasibility study. Tech. Rep. NCAR/TN-446-STR, National Center for Atmospheric Research.

Judge, P.G.: 1998, Astrophys. J. 500, 1009. DOI.

Judge, P.G., Carlsson, M.: 2010, Astrophys. J. 719, 469. DOI.

Judge, P.G., Reardon, K., Cauzzi, G.: 2012, Astrophys. J. 755, L11. DOI.

Judge, P.G., Tomczyk, S., Hannigan, J., Sewell, S.: 2019, Astrophys. J. 877, 10. DOI.

Judge, P.G., Tomczyk, S., Livingston, W.C., Keller, C.U., Penn, M.J.: 2002, Astrophys. J. 576, L157. DOI.

Judge, P.G., Tritschler, A., Low, B.C.: 2011, Astrophys. J. 730, L4. DOI.



Eclipse Observations Page 23 of 23 **166**

Kuhn, J.R., Penn, M.J., Mann, I.: 1996, Astrophys. J. 456, L67. DOI.

Lin, H., Penn, M.J., Tomczyk, S.: 2000, Astrophys. J. 541, L83. DOI.

Lipartito, I., Judge, P.G., Reardon, K., Cauzzi, G.: 2014, Astrophys. J. 785, 109. DOI.

Moise, E., Raymond, J., Kuhn, J.R.: 2010, Astrophys. J. 722, 1411. DOI.

Münch, G., Neugebauer, G., McCammon, D.: 1967, Astrophys. J. 149, 681. DOI.

Penn, M.J., Arnaud, J., Mickey, D.L., Labonte, B.J.: 1994, Astrophys. J. 436, 368. DOI.

Penn, M.J., Kuhn, J.R.: 1994, ApJ 434, 807. DOI.

Penn, M.J., Kuhn, J.R.: 1994b, Solar Phys. 151, 511. DOI.

Penn, M.J., Lin, H., Tomczyk, S., Elmore, D., Judge, P.G.: 2004, Solar Phys. 222, 61. DOI.

Sakurai, T.: 2017, Proc. Japan Acad. Ser. B 93, 87. DOI.

Samra, J.E.: 2018, PhD thesis, Harvard University.

Samra, J.E., Judge, P.G., DeLuca, E.E., Hannigan, J.W.: 2018, Astrophys. J. 856, L29. DOI.

Samra, J.E., Judge, P.G., DeLuca, E.E., Hannigan, J.W.: 2019, Astrophys. J. Lett. 873, L25. DOI.

York, T., Powell, S.B., Gao, S., et al.: 2014, Proc. IEEE 102, 1450. DOI.

Zaitsev, V.V., Shibasaki, K.: 2005, Astron. Rep. 49, 1009. DOI.

